Title
4D Proxy Imaging of Fracture Dilation and Stress Shadowing Using Electrical Resistivity Tomography During High Pressure Injections Into a Dense Rock Formation

Journal
Journal of Geophysical Research: Solid Earth, 126(11)

ISSN
2169-9313

Authors
Johnson, TC
Burghardt, J
Strickland, C
et al.

Publication Date
2021-11-01

DOI
10.1029/2021jb022298

Peer reviewed

4D Proxy Imaging of Fracture Dilation and Stress Shadowing Using Electrical Resistivity Tomography During High Pressure Injections into a Dense Rock Formation

T.C. Johnson[1], J. Burghardt[1], C. Strickland[1], H. Knox[1], V. Vermeul[1], M. White[1], P. Schwering[2], D. Blankenship[2], T. Kneafsey[3] and the EGS Collab Team

[1]Pacific Northwest National Laboratory, USA

[2]Sandia National Laboratory, USA

[3]Lawrence Berkeley National Laboratory, USA

Corresponding author: Tim Johnson (tj@pnnl.gov)

Key Points:

- Time-Lapse 3D ERT imaging is used to monitor stress natural induced fracture dilation and contraction during high pressure injections
- High temporal resolution reveals fine details of complex dynamic poroelastic system behavior during and after injection
- Results demonstrate the potential of ERT for remote, proxy monitoring of changes in stress and fracture aperture in fractured-rock systems

Abstract

Fluid flow through fractured rock systems is governed in large part by the distribution, interconnectivity, and size of fracture apertures. In-situ stress is one of the primary factors controlling fracture aperture, and one that is altered significantly during high-pressure fluid injections or extractions. Interactions between stress, pore pressure, aperture, and fluid flow can result in complex and evolving poroelastic behavior with significant implications regarding the predictability and risk involved with developing and managing deep subsurface reservoirs (geothermal, fossil energy, and geologic carbon sequestration).

In saturated rocks, bulk electrical conductivity is sensitive to both primary and secondary porosity (i.e. matrix porosity and fractures), and therefore to fracture aperture size and distribution. We demonstrate the use of time-lapse 3D electrical resistivity tomography for remotely monitoring stress induced changes in aperture distribution during high pressure injections into a dense fractured rock system at a scale of tens of meters. Results reveal a complex and continuously evolving stress field involving aperture dilations in the natural fracture system and aperture contractions in adjacent zones of shadow stress. Results provide information about the spatiotemporal changes in the system behavior and point to the potential of electrical imaging for autonomously and remotely monitoring evolving stress conditions by proxy through changes in bulk electrical conductivity.

Plain Language Summary

The state and evolution of the stress exerted on rocks has a governing influence on how fluids migrate through deep, fractured rock systems. Dynamic changes in stress during subsurface fluid injections and extractions are difficult to observe, which limits the ability to optimize management of subsurface reservoirs. We demonstrate how time-lapse 3D (i.e. 4D) electrical geophysical imaging can be used to monitor how fractures expand and contract in response to stresses induced during high-pressure injections into a deep fractured-rock formation. Results point to the potential of autonomous electrical imaging for providing actionable feedback information during reservoir operations, enabling enhanced understanding and control.

1 Introduction

Understanding the state and evolution of subsurface stress is critical for developing effective strategies for extracting geothermal and fossil energy resources, sequestering carbon in geologic repositories, managing the risk of induced seismicity, and protecting the environment (U.S. Department of Energy, 2015). Subsurface energy production and carbon sequestration objectives require adequate understanding and control of subsurface fluid flow. The hydrogeologic properties that govern fluid flow are altered by significant changes in stress state (Zoback and Byerlee, 1975, Min *et al.*, 2004, Ito and Hayashi, 2003). For example, during reservoir stimulation injections, deformations caused by changes in fluid pressure can cause existing fractures to open, close, or shear even at locations away from, and without direct hydraulic connection to the injected fluid. Interactions between stress and hydraulic properties often result in complex and evolving fluid flow fields both during and after fluid injections and extractions. Understanding these site-specific interactions over time will enable improved understanding and control of stress-sensitive fractured rock flow systems.

Current technologies are unable to directly measure the initial state of stress or to monitor for changes in stress over time. Instead, stress metrics are inferred from proxy observations such as strain (Murdoch *et al.*, 2020), micro-seismic event locations, borehole breakouts (Zoback *et al.*, 2003), pressure and flow observations during hydraulic fracturing, and earth displacements (White *et al.*, 2014). Each method has its own advantages and disadvantages. For example, micro-seismic event locations can provide real-time information concerning where and when changes in the stress field occur, but sometimes even large changes in stress generate few events while other times even small changes in stress generate many events. The exact mechanism responsible for micro-seismicity remains poorly understood (Eyre *et al.*, 2019). Therefore, micro-seismic monitoring alone provides at best an incomplete understanding. Borehole breakouts and over-coring provide useful information concerning the state of stress at a point in the borehole at a given time but not on the evolution of stress during fluid injection and extraction. Pressure and flow observations during fracturing provide some information on minimum principal stress magnitude, and together with subsequent image logging some information on stress orientation, but is generally not reliable at determining the other two principal stresses (Lakirouhani *et al.*, 2016), nor information about spatial variations in the stress field away from the well. Ground surface deformation measurements can provide some information about the deformation induced by subsurface injection or production but lack sensitivity to uniquely image deep subsurface changes and suffer from decreased resolution as the depth of the target increases (Vasco et al 2000). Borehole-based measurements of strain and tilt can offer high sensitivity but are expensive to deploy and therefore generally uncommon and too sparse to provide a complete inverse solution (Murdoch et al., 2020).

In this paper, we demonstrate the use of time-lapse electrical resistivity tomography (4D-ERT) for monitoring when, where, and how changes in stress modulate secondary porosity (i.e. fracture apertures) during high pressure injections into a dense metamorphic rock formation. ERT is a geophysical method of remotely imaging the spatial distribution of subsurface bulk electrical conductivity (BEC), which is sensitive to stress induced porosity variations in dense (i.e. crystalline and metamorphic) saturated rocks (Brace *et al.*, 1965, Brace and Orange, 1968, Brace

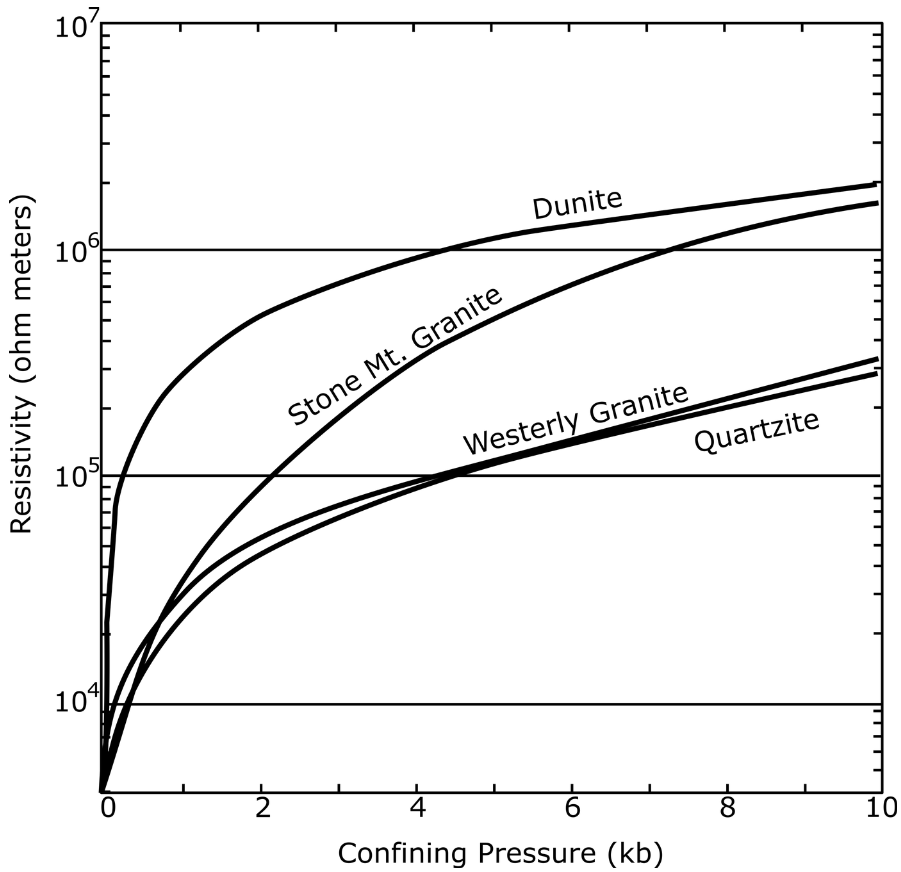

Figure 1. Resistivity vs. confining pressure for several saturated crystalline rock samples. Testing was conducted at constant pore pressure and fluid conductivity. From Brace, W.F. & Orange, A.S., 1966. Electrical Resistivity Changes in Saturated Rock under Stress, Science, 153, 1525-&. (DOI: 10.1126/science.153.3743.1525) Reprinted with permission from AAAS.

and Orange, 1966). To illustrate, Figure 1 shows results from an early study by Brace and Orange (1966) where bulk electrical resistivity (the reciprocal of BEC) was measured with respect to confining pressure on several crystalline rock samples.

During these tests fluid conductivity and pore pressure were held constant as each sample was exposed to increasing levels of confining pressure. The resistivity versus confining pressure curves initially show sharp rates of increase that gradually reduce with increasing confining pressure. Noting that a significant fraction of current flow in saturated crystalline rock occurs by ionic conduction through fluid-filled void spaces (both connected and disconnected), they attributed this behavior to a reduction in porosity with increasing confining pressure. Follow-on studies demonstrated decreasing resistivity (increasing BEC) caused by increasing secondary porosity during shear induced dilatancy of saturated crystalline rocks (Wang *et al.*, 1975, Brace, 1975). The general shape of the resistivity vs. confining pressure relationship can be described using the concept of compliant and stiff porosity (Shapiro, 2003, Mavko and Jizba, 1991). Compliant, or soft porosity corresponds to void spaces with large aspect ratios (the ratio of the maximum to the minimum dimension of the pore) such as fractures, where stresses exerted normal to the long axis result in relatively large strain. Stiff porosity corresponds to void spaces that are more-or-less isometric in shape. Referring to Figure 1, compliant void space is the first to be compressed with increasing confining pressure, resulting in a relatively large decrease in porosity and concomitant large increase in resistivity. As confining pressure increases, compliant void spaces close and the porosity vs. stress relationship is increasingly governed by stiff porosity; hence the sensitivity of porosity and resistivity to confining stress decreases. The relatively large fraction of compliant porosity versus stiff porosity in fractured crystalline rocks explains the high sensitivity of resistivity to stress in comparison to sedimentary rocks, which generally have higher fractions of stiff porosity, despite having generally lower overall elastic stiffness. For example, Lockner and Byerlee (1985) noted a decrease in BEC of 94% for a granite sample and 24% for a sandstone sample, each exposed to 200 MPa (2 kilobar) confining pressure. In general, this same stress/porosity mechanism governs stress-dependent elastic properties and seismic velocity in saturated rocks, except that resistivity is markedly more sensitive (Wilt and Alumbaugh, 2003, Kaselow and Shapiro, 2004).

The sensitivity of secondary porosity to stress in dense fractured rock systems provides the opportunity to use ERT to remotely monitor aperture evolution, particularly in the compliant porosity stress regime below approximately 200 MPa where most subsurface energy and storage operations occur. Under saturated conditions with constant temperature and pore fluid conductivity, transient changes in BEC are governed by changes in porosity and may therefore be used as proxy metrics for monitoring stress induced changes in fracture apertures and for corresponding inferences regarding the evolution of stress.

The advantages of using ERT for this purpose are numerous. 1) ERT arrays are composed only of electrical conductors (i.e. copper wires) and electrodes, and require no moving parts. With appropriate design robust systems can be deployed in high pressure and temperature environments with long-term survivability. 2) ERT arrays can be installed behind casing. 3) ERT monitoring data can be collected continuously and autonomously, making it ideal for time-lapse monitoring applications. 4) 4D ERT imaging can be executed real-time (Johnson *et al.*, 2018, Johnson *et al.*, 2015), providing operators with actionable feedback during operations. 5) ERT monitoring can be conducted in 1D, 2D, or 3D depending on available electrode deployments. 6) Under constant porosity conditions, ERT can be used to monitor the migration of fluids, providing those fluids have contrasting conductivity to native pore fluids (Singha *et al.*, 2015). The primary disadvantage of ERT is that it cannot be co-deployed with uncoated metallic wellbore casing or other electrically conductive infrastructure, which is used ubiquitously in energy-related applications.

In this paper we demonstrate the use of 4D ERT monitoring during high-pressure flow testing within a hydrofractured, highly instrumented, well-characterized meso-scale metamorphic rock test bed, located in a former gold mine approximately 1.5 km beneath the ground surface (Schoenball *et al.*, 2020, Fu *et al.*, 2021). 3D ERT surveys were collected every 34 minutes during a 13-day test sequence consisting of variable pressure and flow injections into the hydro-fractured interval of a borehole. Positive changes in BEC from pre-injection conditions are likely caused by pressure induced opening of natural fractures, whose locations are verified through inspection of oriented borehole cores (Fu *et al.*, 2021). Negative changes in bulk conductivity can be explained by increased compressive stresses exerted normal to the faces of pressurized natural fractures, often referred to as the stress shadowing effect (Taghichian *et al.*, 2014, Yoon *et al.*, 2015, Zhou *et al.*, 2018, Sobhaniaragh *et al.*, 2019). The evolution of BEC over time shows that the hydrofracture zone intersects the natural fracture system, which then undergoes complex and continuously evolving fracture aperture modulations, even after cessation of injections and depressurization of the injection wellbore. BEC evolution during a shut-in test reveals complex poroelastic behavior where depressurization of the hydro-fracture reduces stress shadowing in some parts of the system, which enables built-up pressure to open fractures in other parts of the system even though wellbore shut-in pressure is decreasing. The imaging results also provide insight into the source of 'plugging' behavior experienced toward the end of the test, showing that an apparent decrease in system permeability occurred near the injection wellbore or within the hydro-fracture, and not within the natural fracture system. In addition, the images confirmed the dominating influence of the natural fracture system in establishing flow from the injection well through the hydrofracture zone to the production well, which was a primary objective of the stimulation and flow testing.

2 Materials and Methods

2.1 Experimental Test Bed

The experimental test bed is located at the Sanford Underground Research Facility (SURF) in South Dakota, United States (Kneafsey *et al.*, 2020). The test bed lies completely within the Poorman Formation, a metasedimentary rock consisting of sericite-carbonate-quartz phyllite (the dominant rock type), biotite-quartz-carbonate phyllite, and graphitic quartz sericite phyllite (Caddey *et al.*, 1991), with primary porosity less than 1% on average (reference). Eight sub-horizontal boreholes were drilled from a drift located 1478 m (4850 ft) below the ground surface; one injection borehole, one production borehole, and six monitoring boreholes oriented as shown in Figure 2A. The injection and production boreholes were aligned parallel to the anticipated direction of minimum stress so that hydraulic fractures would nominally propagate orthogonal to the injection borehole axis and intersect the production borehole. ERT electrodes, seismic instrumentation, and distributed temperature sensing fiber were deployed on a plastic centralized spine (Figure 2B), inserted into each monitoring borehole, and grouted in place prior to stimulation operations resulting in the electrode array shown in Figure 2A. Electrodes were spaced at 3m in boreholes PST, PSB, PDT, and PDB, and at 2.5 m in boreholes OT and OB.

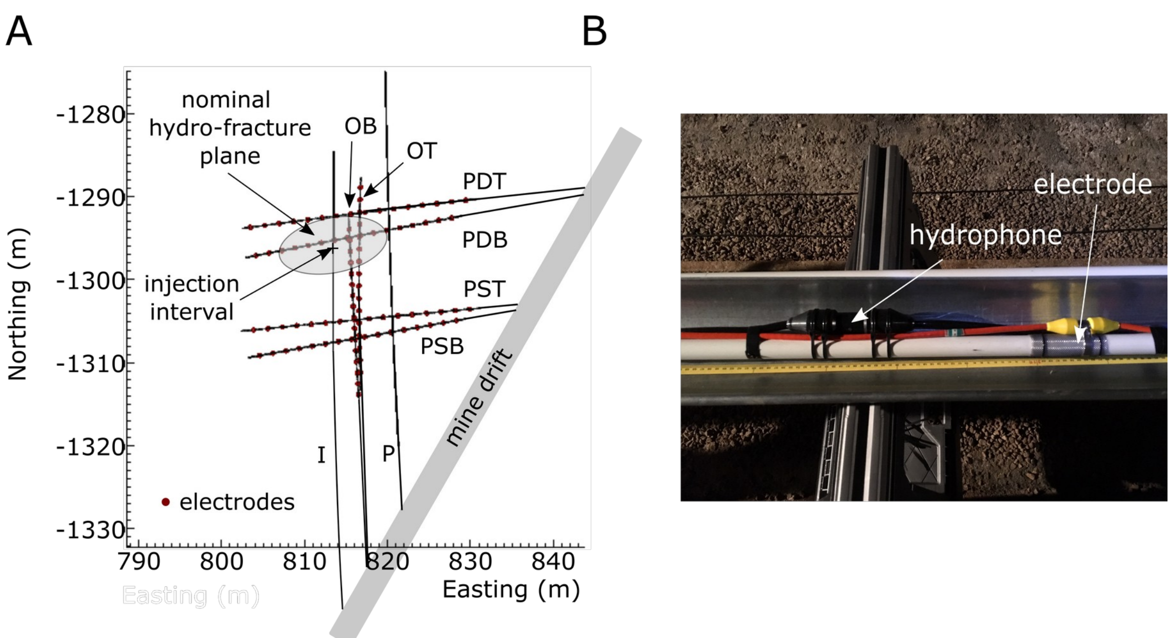

Figure 2. Plan view of the test bed and monitoring string. A) Plan view of injection (I), production (P), and monitoring borehole (OB, OT, PDT, PDB, PST, and PSB) orientations. Each borehole originates at the drift wall and terminates as shown. B)

Photograph of monitoring borehole instrumentation string prior to installation. Each instrumentation string was grouted in place prior to stimulation.

On May 22, 2018 a 1 m interval of the injection borehole (I) centered at 50.3 m (165 ft) from the borehole collar was isolated using a high-pressure straddle packer and stimulated to produce a hydrofracture as shown nominally in Figure 2A. During stimulation, the production borehole was left open to the atmosphere, and high-pressure jet-flow was observed (using a borehole camera) entering the borehole through hairline fractures over an approximately 2m interval near the anticipated hydro-fracture/P-well intersection (Fu et al, 2021). The same injection interval was later re-isolated and used for the flow testing described in this paper.

2.2 ERT Measurements and Inversions

A single ERT measurement is performed by injecting current between two electrodes and measuring the corresponding electrical potential (i.e. voltage) generated between two or more different electrodes. The basic ERT datum used in this paper is the observed potential normalized by the injected current, commonly referred to as the transfer resistance. Many such four-electrode transfer resistance measurements, strategically chosen to optimize imaging resolution, constitute a single ERT survey, which is inverted to produce an imperfectly resolved image of subsurface BEC. In time-lapse ERT imaging, identical surveys are collected on a repeating schedule and inverted to image changes in BEC over time. During the inversion, a discretized representation of the BEC distribution is input into a numerical algorithm, which produces the simulated equivalent of the transfer resistance measurements. The BEC distribution is then updated to reduce the misfit between the observed and simulated transfer resistance measurements, and the process repeats until the observed data are fit within a specified tolerance based on field noise estimates. Isotropic smoothing constraints were used to regularize the inversion in both space and time, such that the only BEC heterogeneity in the inverse images is that which is required to fit the observed data (i.e. Occam's type smoothing constraints). A detailed description of the parallel ERT inversion algorithm and software used to process the ERT data is given in Johnson *et al.* (2010).

Two sources of metallic infrastructure were observed to influence the ERT data. First, the mine drift walls were lined with steel mesh that was fastened to the walls and ceiling with metallic rock bolts (i.e. ground control). We assumed this resulted in a constant potential condition on the drift walls and back. Second, the straddle packer system installed in the injection well (I) was supplied using stainless steel tubing, which was electrically coupled to the formation through the water in the borehole. We assumed this resulted in a constant potential condition for the length of the injection borehole above the packer. Effects of the conductive mesh in the drift and the conductive tubing in the injection borehole were simulated as part of the inversion process using the approach described in Johnson and Wellman (2015), which resulted in a significant improvement in data fit and image interpretability (White *et al.*, 2019). Data described in this paper, including both raw data and input files for the time-lapse inversion are available at https://dx.doi.org/10.15121/1651116 . The parallel code used to process the data is available in open source and may be obtained at https://e4d.pnnl.gov.

2.3 Baseline Test Bed Characterization

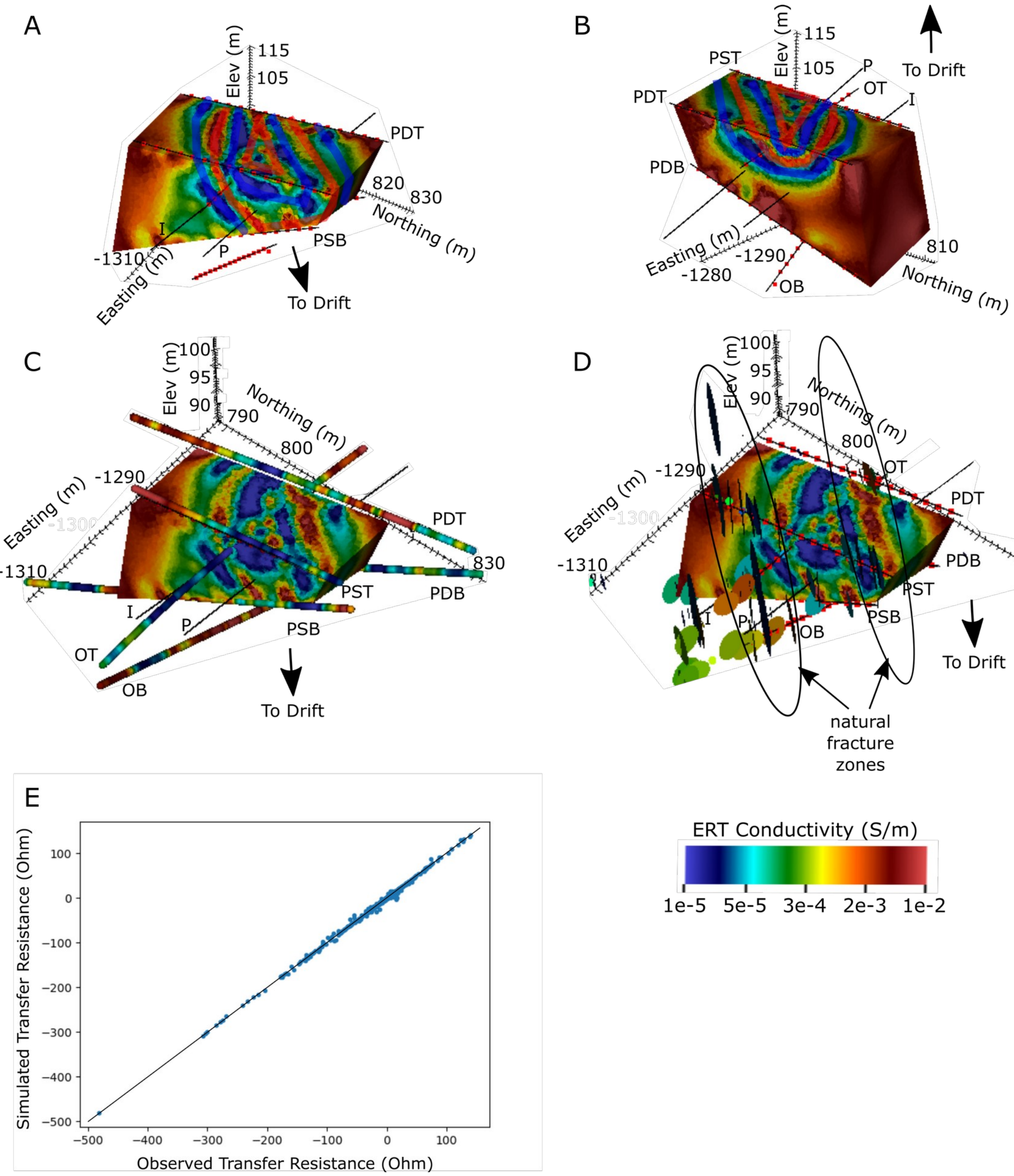

Figure 3. Pre-stimulation images of electrical conductivity and natural fracture patterns. A) Image of baseline BEC from southeast to northwest and B) northwest to southeast . Red and blue transparent lines are added to emphasize folded and dipping layers of continuous BEC C) Comparison of ERT derived BEC and borehole conductivity logs. D) Comparison of BEC structure and natural fracture patterns identified through inspection of continuous oriented core. Identified fractures are represented as disk shapes with strike and dip equivalent to that of the fracture. The two fracture zones identified are visible on the drift wall and are assumed to be prevalent within the testbed. E) Simulated vs. Observed ERT data for baseline inverse solution.

After stimulation and subsequent hydraulic characterization testing (White *et al.*, 2019), the system relaxed for approximately 3 months before 3D baseline ERT data were collected using a series of 1498 in-line and cross-hole dipole-dipole measurements. Based on noise analysis of repeat measurements, 1068 of those data were used to estimate the BEC structure of the testbed.

Figures 3A and 3B show different view angles of the baseline ERT inversion and reveal that the testbed lies within a series of folded and dipping layers of alternating high and low BEC. The transparent blue and red lines are added to emphasize the conductivity structure. Figure 3C shows a comparison of the baseline ERT image and borehole resistivity logs (plotted as BEC along each borehole) that were collected prior to monitoring borehole grouting. The resistivity logs provide a second line of evidence regarding the true BEC structure and agree well with the baseline ERT image considering the relatively high 1D resolution provided by the logging tool compared to the lower 3D resolution provided by ERT inversion.

Continuous cores were collected along each borehole during drilling. Cores were oriented upon extraction by comparison with oriented borehole image logs. The image logs and cores were inspected to identify existing natural fractures and their orientations. Figure 3D shows the resulting natural fracture patterns superimposed on the baseline ERT image. Dominant fracture orientations are mostly aligned with the BEC structure, suggesting that natural facture patterns and BEC are related to the same rock properties and/or formative processes. In addition to oriented core inspection, several lines of evidence support the existence of two dominant natural fracture zones oriented as shown in Figure 3D. White precipitates are visible along the drift wall and ceiling at the projection of the southeastern-most fracture zone to the drift. During the drilling of monitoring well OT, drilling fluids entered the production well (P) and caused it to flow when the drilling had advanced to the northeastern-most fracture zone, suggesting an open fracture(s) connecting well OT and well P. Furthermore, after a long period of flow into the stimulated injection well interval (conducted after the flow testing discussed in this paper), water began to seep from the drift wall and back at the projection of the northeastern fracture zone to the drift.

Figure 3E shows a comparison of the observed and simulated transfer resistance measurements (see section 2.2) at convergence of the baseline inversion. Each time-lapse data set described in the following sections was weighted identically to the baseline data set and fit to the same tolerance as shown in Figure 3E.

3 Hydro fracture flow testing sequence and ERT monitoring data

On Oct. 24, 2018, after the 3-month rest period, a thirteen-day test sequence was initiated with the injection interval isolated using high pressure straddle packers and pressured with water to open the hydro-fracture(s) and induce flow within the test bed. The production well was left open to the atmosphere. Injected water consisted of mine supply water at a constant specific conductance of approximately 0.7 mS/cm. Produced water extracted from the production borehole was measured at approximately 2.0 mS/cm initially and reduced over time, varying from approximately 0.9 to 1.5 mS/cm after about 3 days of continuous injection. We assume from these measurements that injected water was lower in specific conductance than native pore water, which is important when interpreting the time lapse ERT images. Specifically, increases in BEC over time cannot be caused by the transport of injected water through the system, because injected water has a lower specific conductance than native pore water.

ERT surveys were collected every 34 minutes for the duration of the test sequence, each survey being identical to the baseline survey of 1068 measurements. Figures 4A-F show the injection interval pressure and flowrate history, along with the corresponding transfer resistance time series for four of the 1068 measurements used in the inversion, each chosen to illustrate the observed transfer resistance response to flow and pressure in different regions of the testbed. The resistance time-series in Figure 4A-C correspond to electrode locations shown in Figure 4G-J, which also show the sensitivity patterns of transfer resistance to BEC for the same measurements.

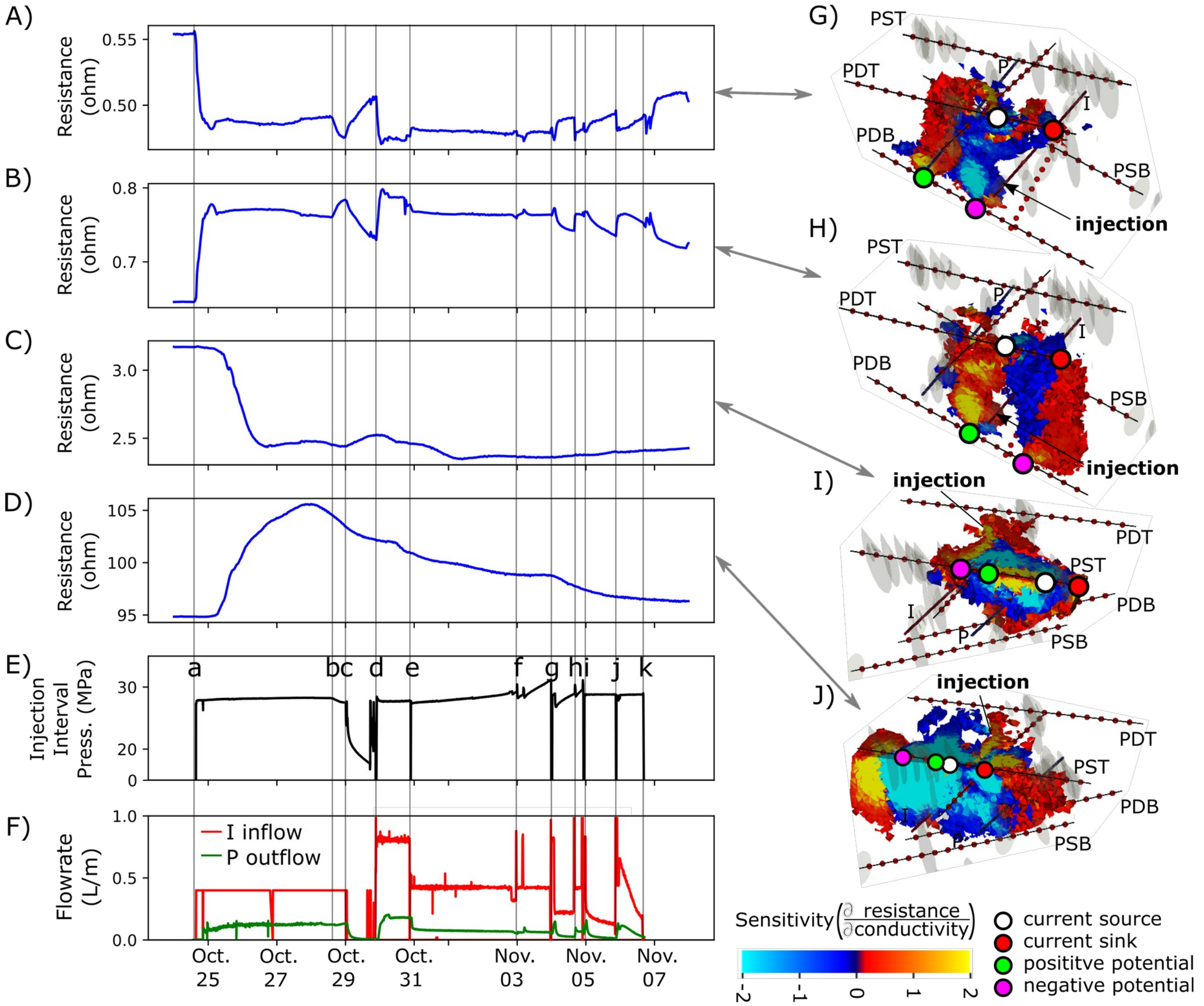

Figure 4. (A-D) Example ERT data time-series with respect to E) injection interval pressure and F) injection and production flow rate. The time-series in A-D correspond to the electrode positions in (G-J). Vertical lines are provided as an aid to align times of notable events between plots. (G-J) Sensitivity distribution of the change in observed transfer resistance with respect to the change in BEC for measurements A-D respectively. An increase in BEC within a region of positive sensitivity (warm colors) will cause an increase in transfer resistance and vice versa. Note that the injection interval in Figures 4I and 4J is obscured by the sensitivity map.

Sensitivity is the derivative of the transfer resistance with respect to BEC and expresses the change in transfer resistance that would be caused by a change in BEC from baseline conditions at each location of the testbed. Sensitivities are computed and used by the inversion to estimate the BEC, and their inspection provides insight into the possible locations of changes in BEC that cause the corresponding changes in transfer resistance shown in Figures 4A-D. Increases in BEC in regions of positive sensitivity will cause an increase in transfer resistance and vice versa. For example, the sharp decrease in transfer resistance at the onset of pumping for the measurement in

Figure 4A is caused by either an increase in BEC (compared to baseline BEC) in the blue sensitivity region, or a decrease in BEC within the red sensitivity region of Figure 4G. Since the hydrofracture exists within the blue region, the sharp response is likely caused by the hydrofracture opening at the onset of pumping, resulting in an increase in porosity and BEC. As described in more detail below, Figures 4B and 4H support the same conclusion.

3.1 Pressure and Flow Time Series

A summary of the injection interval pressure and flowrate over the test period is shown in Figures 4E-F and described in Table 1. One objective of the test was to establish consistent, predictable, and repeatable flow between the injection (I) and production (P) wells. However, increases in injection interval pressure were observed during constant flow rate testing conducted after Oct. 31 (Figure 4E).

Table 1. Summary of flow test sequence and observations injection interval flow and pressure (see Figure 3E-F).

Test Interval	**Description**
a-b	Constant rate injection test at 0.40 L/m.
b-c	Continuation of a-b with anomalous decrease in injection interval pressure
c-d	Shut-in test. Flow is stopped and injection interval pressure is shut in. Two brief flow tests followed by shut-in occurred at the end if this test interval.
d-e	Constant rate injection test at 0.80 L/m.
e-f	Constant rate injection test at 0.40 L/m. Gradual build-up of injection interval pressure observed.
f-g	Two short-duration higher-flow rate tests (0.8 L/m) followed by followed by a 0.4 L/m constant flowrate test. Build-up of injection interval pressure observed.
g-h	Short duration higher-flowrate test (1 L/m) followed by lower flowrate test at 0.2 L/m. Build-up in injection interval pressure observed.
h-i	Short duration high flowrate injection (1 L/m) followed by short-duration constant flow-rate test at 0.4 L/m. Build-up in injection interval pressure observed.
i-j	Short duration high-flowrate (1 L/m) injection followed constant interval

	pressure injection test. Decrease in flowrate observed.
j-k	Short duration high-flowrate (1 L/m) injection followed constant interval pressure injection test. Decrease in flowrate observed.

This pressure build-up was alleviated by subjecting the system to short duration, high flowrate injections (e.g. see beginning of test interval g-h in Figures 4E-F), but interval pressures continued to increase over time during subsequent constant rate injections. During constant pressure testing (Figures 4E-F interval i-j and j-k), injection flow rates decreased over time. As will be shown, the BEC time-series provide some insight regarding the mechanisms governing this flow and pressure behavior.

3.2 Resistance time-series and sensitivities

The electrode positions for the resistance time-series shown in Figures 4A-D are shown in Figures 4G-J. These measurements were chosen to illustrate transfer resistance behavior for measurements that are sensitive to different parts of the system, both near to and far from the stimulated hydro-fracture. Time-series A and B show high sensitivity to the anticipated hydro-fracture region as shown in Figures 4G-H. Changes in transfer resistance are highly correlated and responsive to changes in injection interval pressure and flowrate. The sensitivity patterns for measurements A and B provide insight into to the mirror-image form of each time-series. Consider the sensitivity patterns in the region between two vertical planes passing through the axis of boreholes I and P, near the PDT-PDB plane (i.e. the location of the hydrofracture). The sensitivities in this region for measurement A and B are similarly distributed but are respectively negative-valued and positive-valued. An increase in BEC caused by the hydrofracture opening at the onset of pumping could reasonably cause the decrease in transfer resistance observed in measurement A and the increase in transfer resistance in measurement B. This region is also directly aligned with the northeastern fracture zone (Figure 3D) and encompasses the open fracture connecting boreholes OT and P discussed previously.

Measurements C and D are sensitive to regions of the subsurface that are relatively far from the hydro-fracture zone (Figure 4C-D and I-J). These show a delayed response to flow and pressure variations in comparison to measurements A and D. Measurement D exhibits a continuous, relatively slowly varying increase in transfer resistance followed by a decrease after Oct. 28, suggesting a continuous evolution of the test-bed in the sensitive region (Figure 4J) and failure to reach a steady state condition during any of the steady pressure and/or flowrate testing intervals. None of the measurements return baseline conditions for at least 30 hours after depressurization of the injection interval (Figure 4E time k).

4 Time-lapse ERT difference imaging and interpretation

ERT monitoring during the test sequence produced approximately 630 time-lapse surveys. Each time-lapse survey was inverted as described in section 2.2. The baseline inversion shown in Figure 3 was then subtracted from each time-lapse inversion to produce the 3D change in BEC over time. An animation of the BEC difference time series is available at https://dx.doi.org/10.15121/1651116 and in the Supporting Information to this manuscript. Readers should view that animation to understand the full evolution of the BEC field with respect to the injection interval flow and pressure time-series. For discussion, six frames of the BEC difference sequence are shown in Figure 5.

4.1 Onset of pumping to the shut-in test

Beginning with Figure 5A, a zone of increased BEC develops shortly after the onset of pumping in the region where the hydrofracture intersects the northeastern fracture zone (Figure 5A-1), and moves toward the southeast along the natural fracture zone (Figure 5A-2). A second positive anomaly appears in the southwestern fracture zone (Figure 5A-3), and a third positive anomaly develops in between the northeastern and southwestern fracture zones (Figure 5A-4). The primarily line of evidence, suggesting that these increases in BEC are caused by pressure-induced dilation of the natural fracture system, is that the injected pore water specific conductance is lower than the native pore water specific conductance, so the increase in BEC is not likely to be caused by an increase in pore water specific conductance. For this reason, we assert that increases in BEC during the test sequence are caused by pressure induced dilation of the natural fracture system. The positive anomaly in Figure 5A-4 appears to be associated with the dilation of one or more ‘dead-end’ fractures. These fractures show expression in the cores from boreholes P, PSB and OT, but no expression at the northern trajectory in boreholes PDT and PDB. A single negative anomaly also begins to develop (Figure 5A-5) adjacent to the dilated fractures in the northeast fracture zone (Figure 5A-1,2). As described below, we assert this anomaly is caused by a compressive stress-induced reduction in porosity.

Figure 5B suggests that the pressure front continues to advance down the northeastern fracture zone to the southeast (Figure 5B-2), and likely out of the ERT imaging volume to the northwest (Figure 5B-1), causing a corresponding dilation of natural fractures and an increase in BEC. The positive anomalies in Figure 5B-3,4 also continue to grow in comparison to time A. The zone of decreased BEC (Figure 5B-5) grows significantly from time A to time B. This negative conductivity anomaly could conceivably be caused by the migration of injected water. However, as detailed in the next section, its evolution over time, particularly its response to injection borehole pressure and its spatial and temporal relationship with dilated zones, suggest it is caused by stress induced porosity reduction, or stress shadowing.

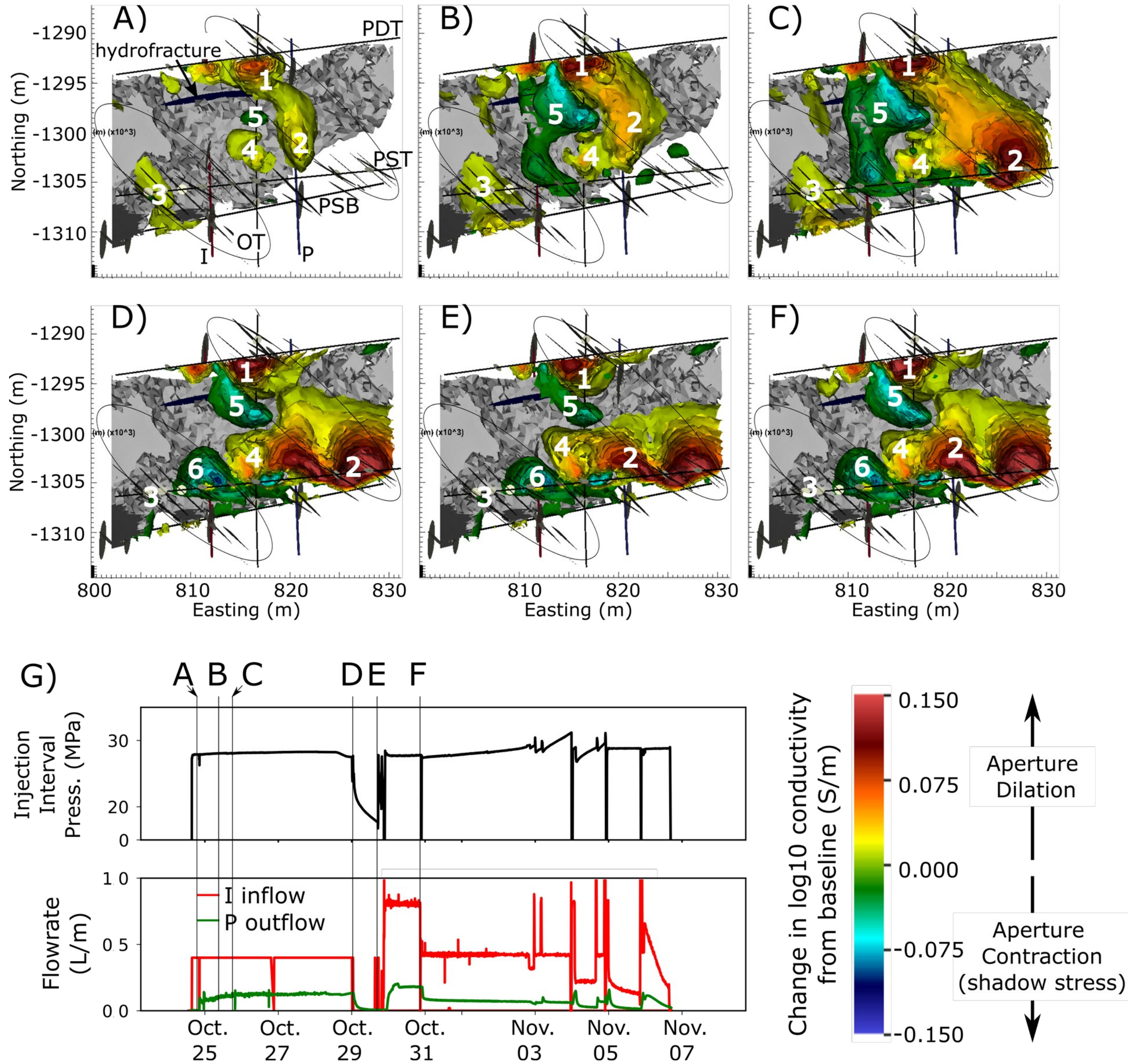

Figure 5. Subset of the 3D time-lapse ERT imaging results at selected times shown in plan view. A-F shows iso-surfaces of the change in BEC from baseline conditions at the times indicated by the vertical lines in G. G shows injection interval pressure and flowrate, as well as the produced water flowrate from wellbore P. The gray region in A-F shows the elements of the computational mesh exhibiting relatively poor resolution where inversion results are not shown. Natural fractures identified in wellbores are shown as black disks at the identified strike and dip. Known natural fracture zones are circled in black. Regions of increased conductivity indicate an increase in porosity (i.e. pore/ fracture dilation). Regions of decreased conductivity indicate a decrease in porosity (i.e. stress shadowing, compression induced pore/fracture contraction).

Specifically, as the pressure front advances through and dilates the natural fracture system, stresses exerted normal to the dilated fracture faces compress the surrounding rock. Figure 5B-5 is 'sandwiched' between the two dilating natural fracture zones (Figure 5B-1,2,3) creating a zone of shadow stress that causes compliant fractures to compress, resulting in reduced porosity and reduced BEC. Figure 5B-4 shows the pressure front migrating outside of the northeastern fracture zone. BEC behavior in this region over time suggests elevated pressure may be moving into a dead-end (either naturally sealed or closed by shadow stresses) natural fracture set. This interpretation is supported by the BEC response during the shut-in test described in the forthcoming discussion. As in Figure 5A-3, fracture dilation at Figure 5B-3 suggests the hydrofracture extended westward far enough to intersect and pressurize the southwestern fracture zone.

At time C the pressure front has migrated downward and dilated the northeastern fracture zone to wellbore PST (Figure 5C-2), causing an increase in the size of the adjacent compressed zone (Figure 5C-5). Pressure and dilation increase in Figure 5C-3,4 in comparison to time B. Pressure build-up/dilation continues into time D such that pressure buildup in the presumed dead-end fracture zone (Figure 5D-4) begins to open and bifurcate the compressed zone (Figure 5D-5,6). This increases the stress on the southwestern lobe of the compressed zone (Figure 5D-6) in comparison to time C which exerts compressive stress on the dilated fractures in the southwestern fracture zone (Figure 5C-3), causing them to return to near baseline aperture conditions (Figure 5D-3), and causing the associated high conductivity anomaly visible at times A, B and C to vanish.

4.2 Shut-in test response

Times D and E are respectively just before and just after a shut-in test, when injection flow is stopped and the injection well pressure is shut in. As pressure dissipates, both the high and low bulk conductivity anomalies decrease in magnitude (Figure 5E-1,2,5,6), suggesting dilated and contracted fractures are moving toward their baseline state; except for the presumed dead-end fracture zone (Figure 5E-4). In this region, the dilated zone advances slightly to the northwest during shut in. This can be explained by a decrease in hydraulic permeability that occurs when pore pressure is reduced and fracture apertures contract at the point where hydrofracture intersect the production well (Figure 5E-1). Without a direct hydraulic connection and pressure release to the production well, elevated pressure within the northeastern fracture zone (Figure 5E-2) diffuses to the northwest into the presumed dead-end fracture zone (Figure 5E-4). This poroelastic behavior seems to be the only plausible explanation for the expansion of the dilated zone during the shut-in test and suggests that fracture closure in the dead-end fractures is caused, in part at least, by stress shadowing. To further illustrate, comparison of Figures 5D-1 and 5E-1 suggests a decrease in dilation (and therefore pressure) where the hydrofracture intersects the northeastern fracture zone at the end of the shut-in test. There is corresponding reduction in compression within the shadow stress zones (Figures 5E-5,6). This reduction in compressive stress causes fractures between the compressed lobes to dilate at Figure 5E-4 (being fed by back-pressure from the dilated zone, Figure 5E-2) even though injection wellbore pressures are decreasing (Figure 5G).

5.3 Higher flow rate test and subsequent flow restrictions

Time F (Figure 5G) is at the end of a higher flowrate (0.8 L/m) injection test conducted after the shut-in test. Regardless of the doubled flowrate, injection interval pressure was approximately equivalent to the previous 0.4 L/m injection test (time D), and stress conditions suggested by the change in BEC were also similar (e.g. compare Figures 5D and 5F).

426 After the 0.8 L/m flowrate test ending approximately Oct. 31st, flowrate was reduced to 0.4 L/m.
427 At this point the testbed began to exhibit behavior where injection interval pressure continuously
428 increased during constant flowrate injections, and flowrate continuously decreased during
429 constant pressure injections. It was observed that the system could be ‘reset’ to some degree by
430 short, high flowrate injections, after which the injection pressure required to achieve a given
431 flowrate was reduced (see pressure and flowrate sequence after Oct. 31st in Figure 6G). The
432 observed increases in injection pressure at a constant flowrate, and decreases in flowrate at a
433 constant injection pressure, indicating an apparent continuous reduction in system permeability.
434 The BEC difference images shown in Figure 6 offer some insight into the location of the
435 permeability reduction.
436

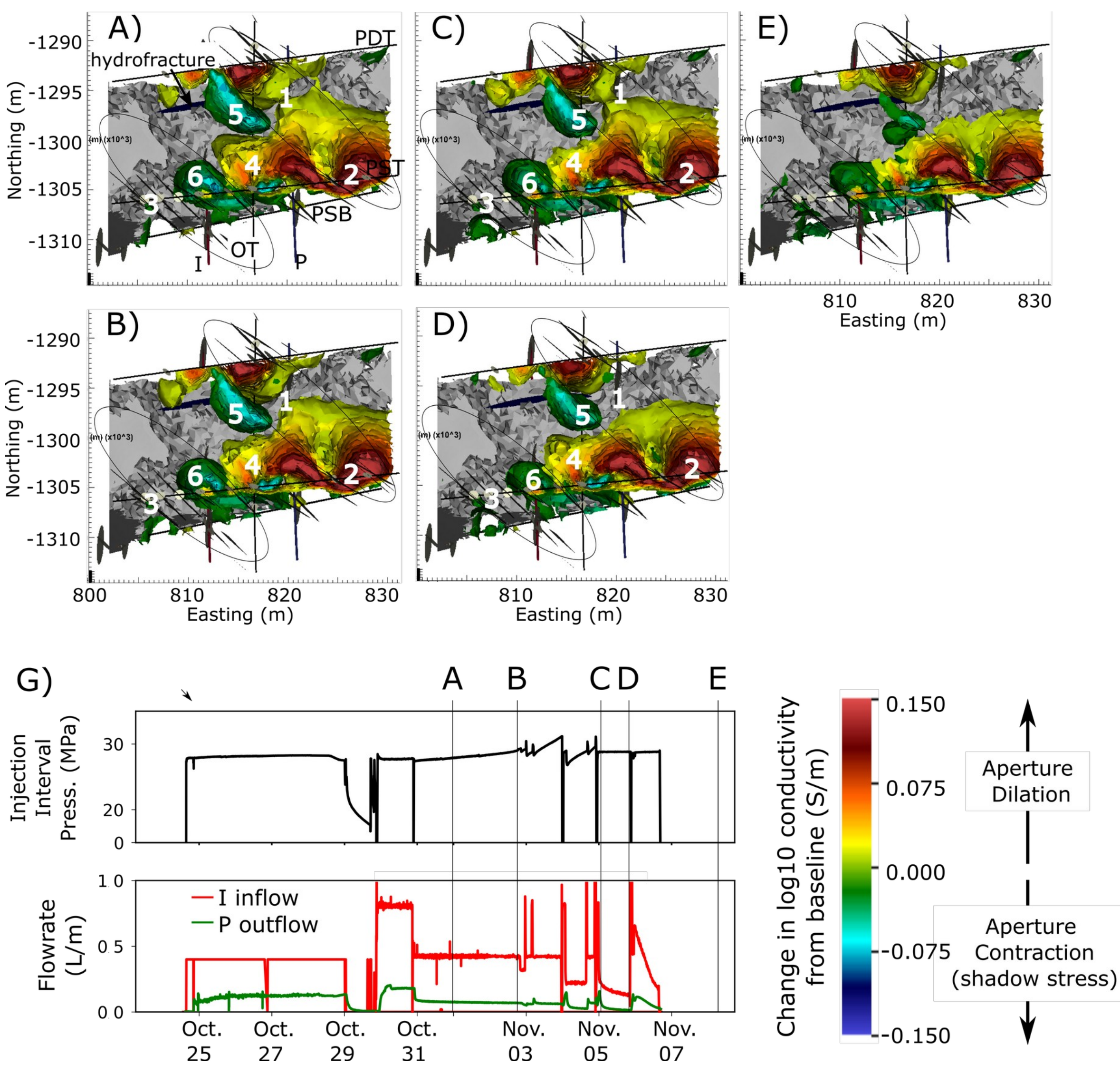

Figure 6. Subset of the 3D time-lapse ERT imaging results at selected times shown in plan view. A-D show iso-surfaces of the change in bulk conductivity from baseline conditions at the times indicated by the vertical lines in G, before (times A and C) and after (times B and D) periods of system permeability reduction. E shows the change in bulk conductivity from baseline approximately 30 hours after pumping ended. G shows injection pressure and injection flowrate, as well as the produced water flowrate from wellbore P. The gray region in A-E shows the elements of the computational mesh exhibiting relatively poor resolution where inversion results are not shown. Natural fractures identified in wellbores are shown and black disks at the identified strike and dip. Known natural fracture zones are circled in black. Regions of increased conductivity indicate an increase in porosity (i.e. pore/ fracture dilation). Regions of decreased conductivity indicate a decrease in porosity (i.e. compression induced pore/fracture contraction).

Figures 6A and 6B show the change in BEC from baseline at the beginning and end of a constant flow test that exhibited continuously increasing injection pressure (see Figure 6G-A,B). Figures 6C and 6D show similar images at the beginning and end of a constant pressure test that exhibited continuously decreasing flowrate (see Figure 6G-C,D) . For the A-B time interval, the BEC difference images suggest higher pressures exist in the natural fracture system at the beginning of the test interval than at the end, even though higher injection pressures exist at the end of the test then at the beginning. Specifically, BEC differences are more extensive and larger in magnitude at the beginning of the test than at the end of the test, suggesting dilation in the natural fracture zones and compression in the adjacent shadow stress zones are greater at the beginning of each test then at the end. The differences are subtle, but clearly exist at points 1 and 5 (e.g. compare Figures 6A-1 and 6B-1, and Figures 6A-5 and 6B-5). This suggests that the increasing injection pressures exhibited from time A to time B are not reaching the natural fracture system.

The differences in BEC are less subtle from time C to time D, particularly at points 1, 5 and 6. Decreases in BEC difference magnitudes (both positive and negative) suggests pressure induced aperture openings and shadow stresses have decreased from time C to time D, even though injection pressure remains constant. In addition, just as observed during the shut-in test, the dilated zone at point 4 advances slightly to the northwest, suggesting decreasing pressure in the natural fracture system (compare Figures 6C-4 and 6D-4).

The first comparison (Figures 6A and 6B) demonstrates that pressure is decreasing within the fracture zone at the same time injection interval pressure in increasing from time A to B. The second comparison (Figures 6C and 6D) demonstrates that pressure is decreasing within the fracture zone while interval pressure is held constant (and flow rate is decreasing). These observations suggest the apparent decrease in system permeability with time is not occurring within the natural fracture system, and therefore must be occurring near the wellbore or within the stimulated hydro-fracture.

Figure 6E shows the change in BEC approximately 30 hours after flow is stopped and the injection interval pressure is reduced to atmospheric pressure. BEC anomalies suggest that after 30 hours after injection borehole depressurization, significant pressures remain with the natural fracture system that are causing fracture dilation and exerting adjacent shadow stresses with respect to baseline conditions.

5 Discussion

Our interpretation of time-lapse imaging results assumes that changes in BEC can only be caused by changes in pore/fracture fluid conductivity, changes in porosity, or changes in saturation. Although there are other mechanisms that can alter BEC (e.g. precipitation or dissolution based changes in mineralogy), we assume these are relatively insignificant over the 13-day test period. We also assume the system is fully saturated at the onset of pumping based on a relatively extensive series of stimulation and flow injections that occurred prior to Oct. 24, 2018 (White *et al.*, 2019). In addition, pressure readings from a sealed horizontal wellbore in the same mine was in excess of 6 MPa (~612 m of water) for the duration of the experiment, suggesting the water table is well above the test bed. If this assumption is in error, increases in saturation could conceivably cause the positive BEC anomalies. However, the negative BEC anomalies cannot be explained by decreases in saturation because saturation with respect to baseline conditions is not likely to decrease during injections. Furthermore, the variations in BEC cannot be reasonably attributed to variations in saturation over the full test period. For example, if initial increases in BEC were caused by unsaturated fractures filling with water, we would not expect later decreases in BEC (e.g. during the shut-in test) because there is no mechanism for the fractures to desaturate during shut in. Our interpretation assumes the system is fully saturated for the duration of the test.

As noted in Section 3, injected fluid conductivity was less than native pore fluid conductivity for the duration of the test. Thus, if previous assumptions hold, positive changes in BEC can only be caused by increases in porosity by fracture dilation. With that established, we offer the following arguments for why the negative changes in BEC are caused by shadow stresses and consequent fracture contraction, and not by the transport of injected fluid of contrasting fluid conductivity. First, fluid flow within the natural fracture system is driven by fluid pressure gradients. The same pore pressure increases that cause fracture dilation also drive fluid flow. Thus, we expect injected fluid flow to occur where fractures are dilated, or equivalently where BEC is greater than baseline conditions. Second, the change in BEC within the shadow zones trends from negative to zero during periods of zero flow (e.g during the shut-in test). This can only occur if compressive shadow stresses are reducing in response to pressure dissipation within the natural fracture zones (as presumed) or if, when injection flowrate ceases, more conductive fluids begin to replace less conductive fluids within the shadow zone. That latter is unlikely because there is no flow being induced within the system. Third, if negative BEC anomalies were caused by transport of injected fluids, we would expect to see a connected progression in negative BEC from the hydrofracture outward into the formation. Instead, the negative BEC anomalies are disconnected (see points 5 and 6 in Figures 5 and 6). For these reasons, it is difficult to construct a non-contradictory argument that explains the negative BEC behavior in terms of fluid flow.

Conversely, there are no contradictory or unexplainable responses when interpreting the negative BEC behavior in terms of shadow stress. For example, the shadow stresses occur adjacent to dilating natural fracture zones as expected. They respond sensibly and in concert with dilating zones in response to injection pressures and flow rates. The magnitude of the negative changes in BEC is muted in comparison to positive changes in BEC. This is consistent with the notion that dilating natural fracture zones are more compliant than the less fractured (and therefore less compliant) regions between the natural fracture zones where shadow stresses are manifest.

6 Conclusions

We have demonstrated the capability to monitor, by proxy, the 4D evolution of changes in subsurface stress using time-lapse ERT in deep, decameter-scale, fracture-flow dominated subsurface system. Here, positive changes in ERT-derived BEC are caused by pressure induced dilation of the natural fracture system. Negative changes in BEC are caused by compressive shadow stresses created adjacent to the dilated natural fracture zones. The evolution of BEC during a 13-day injection test into an existing hydrofracture provides detailed information concerning the evolution of fracture dilations and contractions, and thus the evolution of primary fluid flow paths. As ERT is a scalable geophysical sensing method, this work points to the potential utility of ERT in reservoir-scale systems for remotely and autonomously monitoring changes in the state of stress during and after injections and extractions, enabling enhanced, real-time feedback for improved system understanding and control.

Acknowledgments, Samples, and Data

All data meta-data and data necessary to reproduce this work, including raw data files and E4D input and output files, are publicly available at the U.S. Department of Energy Geothermal Data Repository (http://gdr.openei.org/submissions/1324 or https://dx.doi.org/10.15121/1811498). The ERT modeling and inversion code E4D is open source and publicly available at https:/e4d.pnnl.gov. This material was based upon work supported by the U.S. Department of Energy, Office of Energy Efficiency and Renewable Energy(EERE), Office of Technology Development, Geothermal Technologies Office, under Award Number DE-AC05-76RL01830 with PNNL. Sandia National Laboratories is a multi-mission laboratory managed and operated by National Technology & Engineering Solutions of Sandia, LLC, a wholly owned subsidiary of Honeywell International Inc., for the U.S. Department of Energy's National Nuclear Security Administration under contract DE-NA0003525. This paper describes objective technical results and analysis. Any subjective views or opinions that might be expressed in the paper do not necessarily represent the views of the U.S. Department of Energy or the United States Government. The United States Government retains, and the publisher, by accepting the article for publication, acknowledges that the United States Government retains a non-exclusive, paid-up, irrevocable, world-wide license to publish or reproduce the published form of this manuscript, or allow others to do so, for United States Government purposes. The research supporting this work took place in whole or in part at the Sanford Underground Research Facility in Lead, South Dakota. The assistance of the Sanford Underground Research Facility and its personnel in providing physical access and general logistical and technical support is acknowledged, with a special recognition to George Vandine for his dedication to this project and safe guidance underground. We recognize the Stimulation and Flow Working Group team members for their long hours in the field, nearly a mile underground. Without their efforts, dedication and creativity the data and findings in this work would not be possible.

References

Brace, W.F., 1975. Dilatancy-Related Electrical-Resistivity Changes in Rocks, *Pure Appl Geophys,* 113**,** 207-217.

Brace, W.F. & Orange, A.S., 1966. Electrical Resistivity Changes in Saturated Rock under Stress, *Science,* 153**,** 1525-&.

Brace, W.F. & Orange, A.S., 1968. Further Studies of Effects of Pressure on Electrical Resistivity of Rocks, *J Geophys Res,* 73**,** 5407-&.

Brace, W.F., Orange, A.S. & Madden, T.R., 1965. Effect of Pressure on Electrical Resistivity of Water-Saturated Crystalline Rocks, *J Geophys Res,* 70**,** 5669-&.

Caddey, S.W., Bachmann, T.J., Campbell, R.R., Reid, R.R. & Otto, R.P., 1991. The Homestake gold mine, an early Proterozoic ironformation-hosted gold deposit, Lawrence County, South Dakota USA.

Eyre, T.S., Eaton, D.W., Garagash, D.I., Zecevic, M., Venieri, M., Weir, R. & Lawton, D.C., 2019. The role of aseismic slip in hydraulic fracturing-induced seismicity, *Sci Adv,* 5.

Fu, P., Schoenball, M., Ajo-Franklin, J.B., Chai, C., Maceira, M., Morris, J.P., Wu, H., Knox, H.A., Schwering, P.C., White, M.D., Burghardt, J.A., Strickland, C.E., T.C., J., Vermeul, V.R., Sprinkle, P., Roberts, B., Ulrich, C., Guglielmi, Y., Cook, P.J., Dobson, P., Wood, T.D., Frash, L.P., Huang, L., Ingraham, M.D., Pope, J., Smith, M.M., Neupane, G., Doe, T., Roggenthen, W., Horne, R., Singh, A., Zoback, M.D., Wang, H., Condon, K., Ghassemi, A., Chen, H., McClure, M.W., Vandine, G., Blankenship, D., Kneafsey, T.J. & Team, E.C., 2021. Close Observation of Hydraulic Fracturing at EGS Collab Experiment 1: Fracture Trajectory, Microseismic Interpretations, and the Role of Natural Fractures, *Journal of Geophysical Research: Solid Earth,* 126, e2020JB020840.

Ito, T. & Hayashi, K., 2003. Role of stress-controlled flow pathways in HDR geothermal reservoirs, *Pure Appl Geophys,* 160**,** 1103-1124.

Johnson, T.C., Thomle, J., Robinson, J.L., Mackley, R.D. & Truex, M.J., 2018. Stage B Uranium Sequestration Amendment Delivery Monitoring Using Time-Lapse Electrical Resistivity TomographyPacific Northwest National Lab. (PNNL), Richland, WA (United States).

Johnson, T.C., Versteeg, R.J., Day-Lewis, F.D., Major, W. & Lane, J.W., 2015. Time-Lapse Electrical Geophysical Monitoring of Amendment-Based Biostimulation, *Groundwater,* 53**,** 920-932.

Johnson, T.C., Versteeg, R.J., Ward, A., Day-Lewis, F.D. & Revil, A., 2010. Improved hydrogeophysical characterization and monitoring through parallel modeling and inversion of time-domain resistivity and induced-polarization data, *Geophysics,* 75**,** Wa27-Wa41.

Johnson, T.C. & Wellman, D., 2015. Accurate modelling and inversion of electrical resistivity data in the presence of metallic infrastructure with known location and dimension, *Geophys J Int,* 202**,** 1096-1108.

Kaselow, A. & Shapiro, S.A., 2004. Stress sensitivity of elastic moduli and electrical resistivity in porous rocks, *J Geophys Eng,* 1**,** 1-11.

Kneafsey, T., Blankenship, D., Dobson, P.F., Morris, J.P., White, M.D., Fu, P., Schwering, P.C., Ajo-Franklin, J.B., Huang, L., Schoenball, M., T.C., J., Knox, H.A., Neupane, G., Weers, J., Horne, R., Zhang, Y., Roggenthen, W., Doe, T., Mattson, E., Valladao, C. & Team, E.C., 2020. The EGS Collab Project:

Learnings from Experiment 1. *in 45th Workshop on Geothermal Reservoir Engineering*, pp. 15, Stanford University, Stanford CA.

Lakirouhani, A., Detournay, E. & Bunger, A.P., 2016. A reassessment of in situ stress determination by hydraulic fracturing, *Geophys J Int,* 205**,** 1859-1873.

Lockner, D.A. & Byerlee, J.D., 1985. Complex Resistivity Measurements of Confined Rock, *J Geophys Res-Solid,* 90**,** 7837-7847.

Mavko, G. & Jizba, D., 1991. Estimating Grain-Scale Fluid Effects on Velocity Dispersion in Rocks, *Geophysics,* 56**,** 1940-1949.

Min, K.B., Rutqvist, J., Tsang, C.F. & Jing, L.R., 2004. Stress-dependent permeability of fractured rock masses: a numerical study, *Int J Rock Mech Min,* 41**,** 1191-1210.

Murdoch, L.C., Germanovich, L.N., DeWolf, S.J., Moysey, S.M.J., Hanna, A.C., Kim, S. & Duncan, R.G., 2020. Feasibility of using in situ deformation to monitor CO2 storage, *Int J Greenh Gas Con,* 93.

Schoenball, M., Ajo-Franklin, J.B., Blankenship, D., Chai, C.P., Chakravarty, A., Dobson, P., Hopp, C., Kneafsey, T., Knox, H.A., Maceira, M., Robertson, M.C., Sprinkle, P., Strickland, C., Templeton, D., Schwering, P.C., Ulrich, C., Wood, T. & Team, E.C., 2020. Creation of a Mixed-Mode Fracture Network at Mesoscale Through Hydraulic Fracturing and Shear Stimulation, *J Geophys Res-Sol Ea,* 125.

Shapiro, S.A., 2003. Elastic piezosensitivity of porous and fractured rocks, *Geophysics,* 68**,** 482-486.

Singha, K., Day-Lewis, F.D., Johnson, T. & Slater, L.D., 2015. Advances in interpretation of subsurface processes with time-lapse electrical imaging, *Hydrol Process,* 29**,** 1549-1576.

Sobhaniaragh, B., Haddad, M., Mansur, W.J. & Peters, F.C., 2019. Computational modelling of multi-stage hydraulic fractures under stress shadowing and intersecting with pre-existing natural fractures, *Acta Mech,* 230**,** 1037-1059.

Taghichian, A., Zaman, M. & Devegowda, D., 2014. Stress shadow size and aperture of hydraulic fractures in unconventional shales, *J Petrol Sci Eng,* 124**,** 209-221.

U.S. Department of Energy, O.o.S., 2015. Controlling Subsurface Fractures and Fluid Flow: A Basic Research Agenda, eds Pyrak-Nolte, L. J. & DePaolo, D. J. U.S. Department of Energy, Germantown, MD.

Wang, C.Y., Goodman, R.E., Sundaram, P.N. & Morrison, H.F., 1975. Electrical-Resistivity of Granite in Frictional Sliding - Application to Earthquake Prediction, *Geophys Res Lett,* 2**,** 525-528.

White, J.A., Chiaramonte, L., Ezzedine, S., Foxall, W., Hao, Y., Ramirez, A. & McNab, W., 2014. Geomechanical behavior of the reservoir and caprock system at the In Salah CO2 storage project, *P Natl Acad Sci USA,* 111**,** 8747-8752.

White, M.A., Johnson, T.C., Kneafsey, T., Blankenship, D., Fu, P., Wu, H., Ghassemi, A., Lu, J., Huang, H., Heupane, G., Oldenburg, C., Doughty, C., Johnston, B., Winterfield, P., Pollyea, R., Jayne, R., Hawkins, A., Zhang, Y. & Team, E.C., 2019. The Necessity for Iteration in the Application of Numerical Simulation to EGS:

Examples from the EGS Collab Test Bed 1. *in 44th Workshop on Geothermal Reservoir Engineering*, Stanford University, Stanford CA USA.

Wilt, M. & Alumbaugh, D., 2003. Oil field reservoir characterization and monitoring using electromagnetic geophysical techniques, *J Petrol Sci Eng,* 39**,** 85-97.

Yoon, J.S., Zimmermann, G. & Zang, A., 2015. Numerical Investigation on Stress Shadowing in Fluid Injection-Induced Fracture Propagation in Naturally Fractured Geothermal Reservoirs, *Rock Mech Rock Eng,* 48**,** 1439-1454.

Zhou, J., Zeng, Y.J., Jiang, T.X. & Zhang, B.P., 2018. Laboratory scale research on the impact of stress shadow and natural fractures on fracture geometry during horizontal multi-staged fracturing in shale, *Int J Rock Mech Min,* 107**,** 282-287.

Zoback, M.D., Barton, C.A., Brudy, M., Castillo, D.A., Finkbeiner, T., Grollimund, B.R., Moos, D.B., Peska, P., Ward, C.D. & Wiprut, D.J., 2003. Determination of stress orientation and magnitude in deep wells, *Int J Rock Mech Min,* 40**,** 1049-1076.

Zoback, M.D. & Byerlee, J.D., 1975. Effect of Microcrack Dilatancy on Permeability of Westerly Granite, *J Geophys Res,* 80**,** 752-755.